# Spontaneous network transitions predict somatosensory perception

Abhinav Sharma[1,2,3], Joachim Lange[1], Diego Vidaurre[4,5], Esther Florin[1,6]

[1] Institute for Clinical Neuroscience and Medical Psychology, Medical Faculty, Heinrich-Heine University, Düsseldorf, Germany

[2] MRC Brain Network Dynamics Unit, University of Oxford, UK

[3] Nuffield Department of Clinical Neurosciences, University of Oxford, UK

[4] Department of Clinical Medicine, Center of Functionally Integrative Neuroscience, Aarhus University, Aarhus, Denmark

[5] Department of Psychiatry, University of Oxford, Oxford, UK

[6] McGovern Institute for Brain Research, Massachusetts Institute of Technology, Cambridge, MA, USA

## Summary

Sensory perception is essential for transforming incoming information in the brain into targeted behavior. Thus, variations in our perceptions are ubiquitously associated with human behavioral performance. Since our brains are everlastingly active, the question arises whether spontaneous brain activity relates to perceptual variability and subsequent task performance. We analyzed spontaneous whole-brain activity preceding the trials of an ambiguous tactile temporal discrimination task and identified time-resolved brain networks from the seconds before each trial. Transitions to a frontal and a multi-frequency network across the brain were essential for the correct percept. Conversely, incorrect percepts are mainly preceded by transitions to an alpha-parietal network. Moreover, brain switches occur faster during the period before stimulus presentation for correct stimuli detection, suggesting the need for enhanced network flexibility during this phase. Thus, the interaction between whole-brain networks in the spontaneous pre-stimulus period contributes to the perception during the task.

**Keywords:** MEG, spontaneous whole-brain networks, time-resolved activity, coherence, connectivity, tactile perception, perceptual variability

# Introduction

Humans are not constantly engaged in tasks. But even at rest, our brains are buzzing with activity not pertaining to any specific cognitive demand. Compare your daily morning routine over two days. Even if everything remains the same, you will produce variability (good or bad) on one or multiple tasks across the two days. Motor behavior forms most of our daily tasks, most of which involve our hands. Tactile sensory feedback is critical for accurately controlling the fine motor skills executed by human hands. Therefore, tactile perception is crucial for our ability to explore and interact with the world around us. The neural mechanisms of distinct brain areas relevant to tactile perception are relatively well-understood in non-human primates and provide a solid foundation for investigating human perceptual variability[1]. In humans, changes in neural activity within brain regions processing sensory information milliseconds before a task begins correlate with perception[2–8]. While these findings highlight the relevance of specific brain areas during the preparatory period, the interconnection and the temporal interplay between those brain areas in the seconds before tactile perception are unknown. Yet, the interaction and communication between brain areas and whole-brain networks is known to be relevant for cognition, and in addition networks are disconnected in diseases[9].

Whole-brain networks are commonly robustly extracted from minutes of spontaneous data. Time-resolved techniques indicate that our brain at rest switches between networks every 50-200ms[10,11]. This makes it likely that differences in spontaneous network configurations are responsible for perception differences. However, the relevance of whole-brain network configurations for perception or task performance has not yet been demonstrated.

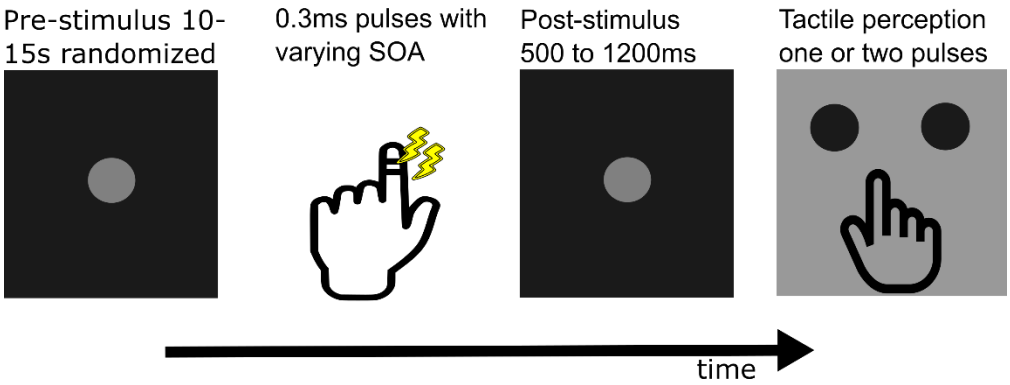


**Figure 1**: Schematic of the task paradigm (see Methods: Tactile discrimination paradigm), which was adapted based on previous studies[5,20]. The presented stimulus onset asynchrony (SOA) varied between 0ms, the critical SOA, critical SOA ± 10 ms, and 3 times the critical SOA.

To gain insights into the relevance of whole-brain networks for tactile perception, participants received two short consecutive tactile stimuli in the form of electric pulses and indicated with a button press the percept of either one or two pulses (Figure 1). This setup induces perceptual ambiguity because short inter-stimulus intervals lead to the perception of only one stimulus despite two being applied. Using a staircase procedure, we determined for each participant the inter-stimulus interval with 50% correct detections of 2 stimuli, which is termed critical *stimulus onset asynchrony* (SOA). Using a data-driven approach on the seconds of electrophysiological spontaneous brain activity before trials with ambiguous percept[10,12], we identified whole-brain network properties and interactions that predict each individual stimulus percept. Our hypothesis was that correct and incorrect detection involve different temporal configurations of the whole-brain networks identified from spontaneous data before the trial starts. Previous studies investigating tactile processing indicate that, among other

brain regions, the fronto-parietal cortices contribute to complex tactile perceptual decision-making (for a review, see ref.[1]). Based on this literature, we focus on fronto-parietal connections with brain regions primarily involved in tactile perception, i.e., sensorimotor cortices, and how temporal evolution of those causes trial-by-trial variability in tactile perception.

In line with the hypothesized relevance of the temporal evolution of whole-brain networks for perception, we identified two distinct whole-brain transition patterns related to either percept. This finding indicates that the literature on the neural mechanisms of human perception needs to include the role of dynamic whole-brain network patterns before a task.

# Results

Using a time-delay embedded (TDE)-Hidden Markov Model (HMM, see methods for details), we computed six networks from the 8 seconds whole brain Magnetoencephalography (MEG) recording preceding stimuli presentation of all critical SOA and critical SOA ± 10ms trials regardless of correct detection.

## Spontaneous pre-stimulus activity organizes into different spectral networks

The HMM resolved the pre-stimulus spontaneous activity into distinct networks with specific spatio-spectral fingerprints. For all six networks, the coherence-based connectivity between different brain regions was visualized for the four main frequency modes (see supplementary Figure 1). Out of the six networks, four networks (network 1 to 4) had diverse spectral and spatial characteristics as well as many frontal, parietal, and sensorimotor connections with various brain regions. Two of these four networks had spectral connectivity restricted to specific yet different spectral bands, and the remaining two displayed multi-frequency spectral connectivity. Because networks 5 and 6 had few frontal, parietal, and sensorimotor connections in any frequency band, we focus mainly on network 1 to 4. We now turn to our four networks of interest and depict their coherence characteristics in the left part of Figure 2.

First, Figure 2a depicts what we term the *cross-brain network* due to its multi-frequency spectral connections. It consisted of an interacting anterior (frontal) and posterior (parietal) network in the alpha, beta, and high-beta/gamma bands. Second, Figure 2b shows the *alpha-parietal network,* which is dominated by alpha band-specific posterior parietal connectivity. In this network, parietal regions were coherent with different brain areas within the parietal cortex and across the brain. Interestingly, there was no robust connectivity within the beta and the high-beta/gamma bands. Third, Figure 2c shows the *frontal network*, which is dominated by multi-frequency spectral coherence in the high-beta/gamma and alpha-band in the frontal and medial-frontal regions. Finally, Figure 2d depicts the *high-beta/gamma network*, which is characterized by high-beta/gamma band coherence between and within frontal and parietal areas. Therefore, within each of the four discussed networks, different brain regions were coherent with the sensorimotor areas to give rise to task-relevant whole-brain networks.

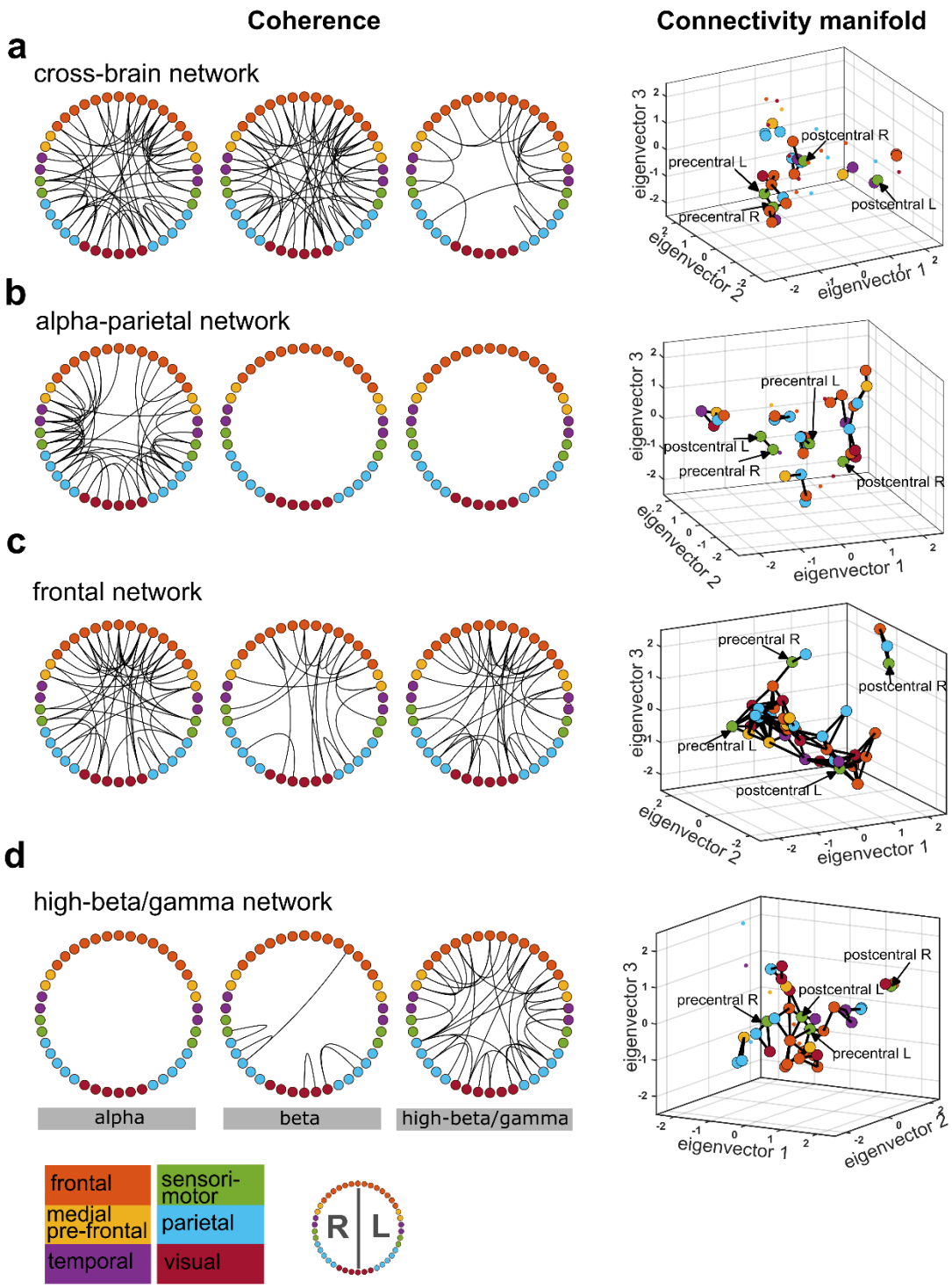


**Figure 2: Coherence and connectivity of the four main networks**

Each dot in the coherence ring and the connectivity manifold represents one of 42 brain areas and is color-coded for the main brain region. The exact brain areas are depicted in supplementary figure 2, and the two further networks are depicted in supplementary figure 3.

**a)** *Cross-brain network*. The connectivity manifold for the cross-brain network indicated connections of the left and right precentral (motor cortices) with the frontal and parietal brain regions.

**b)** *Alpha-parietal network*. This network was characterized by posterior alpha band coherence, but parietal cortex node connectivity was fragmented into different clusters.

**c)** *Frontal network.* Frontal regions were coherent both within frontal cortex regions and to different brain regions across all three frequency bands. This network is densely connected within one main cluster.

**d)** *High-beta/gamma network.* Significant connections were only present in the high-beta/gamma band both within the frontal and parietal regions as well as between the regions. The frontal and parietal regions form a cluster with left post-(somatosensory) and pre-(motor) central gyri.

## Connectivity clusters in the HMM networks

A brain region might operate simultaneously in different frequencies to perform multiple functions, enabling flexibility in the brain region's inputs and outputs[13,14]. Our first result indicated that numerous pairs of brain regions are coherent across several spectral bands within the same network. However, certain brain areas were coherent in identical spectral bands across different networks.

To untangle higher-order interactions within each network, we employed the diffusion map framework on the covariance matrix of each network across the whole spectrum[15,16] (See Methods: Diffusion map analysis for details). The first step involves computing the closeness between brain regions based on the Spearman rank correlation between the covariance vectors of regions. Because this approach accounts for all covariance relationships, it captures higher-order relationships[17–19]. To highlight the essential brain connections for a given network, we reduce the data to a three-dimensional connectivity manifold in a second step. This manifold accounts for direct and indirect connections via multiple brain regions and places regions with greater overall connectivity closer to each other.

The right column of Figure 2 shows the results. First, although the cross-brain network had multi-frequency and spatially non-specific coherence characteristics, only a few brain regions were statistically significantly connected with their neighbors on the cross-brain network's connectivity manifold, indicating an integrative role of this network. Furthermore, the parietal and frontal cortical areas, left motor cortex, and medial orbitofrontal regions were sparsely connected to each other (Figure 2a). Second, the alpha-parietal network's connectivity manifold displayed several disconnected clusters within which at least one parietal region was present. The parietal regions were, however, not connected to the left post-central and right pre-central gyrus (Figure 2b).

Third, for the frontal network, in contrast to the three other networks analyzed, all brain regions were connected to each other in a single cluster, indicating a distributive role of the frontal network. The only exception is the right post-central gyrus, which formed a separate cluster with superior-frontal right and inferior-parietal right (IP-r) gyri (Figure 2c). Of note, in the frontal network, the left and right pre- and post-central gyri were not connected to each other.

Finally, the high-beta/gamma network showed a significant connection between the left pre-central and post-central gyri (Figure 2d and supplementary figure 4b for a 2D view). Like the cross-brain network, the IP-r was connected to the left pre- and post-central gyri via two frontal areas. The left pre- and post-central gyri were further embedded within a cluster of significantly connected frontal regions.

## Differential network transitions indicative of percept

Each brain network described in the previous section has a distinct connectivity profile between the sensorimotor cortices and frontal as well as parietal areas. To test our hypothesis that correct and incorrect stimuli detections involve different temporal configurations of the whole-brain networks during the pre-stimulus period, we examined on a single trial level whether transition probabilities to and from a given brain network significantly differed between correct and incorrect percept trials (see Figure 3).

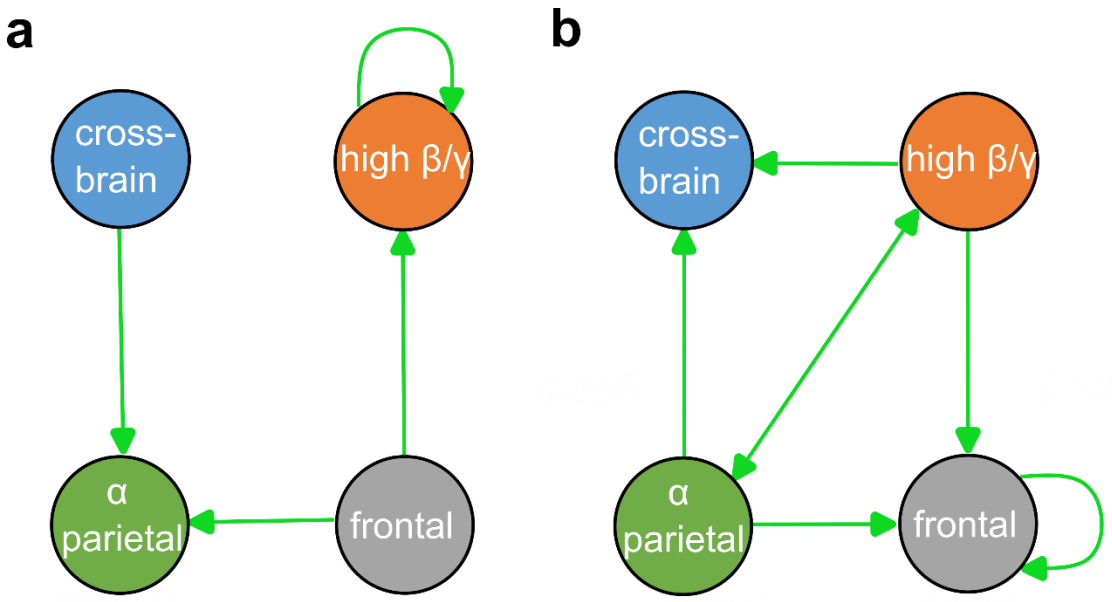


**Figure 3**: **Network transitions preceding the two percepts.**
The arrows indicate significantly increased network transition probabilities between networks at p<0.05. Not depicted transitions were statistically equally likely across percepts.
**a)** Significantly increased network transition probabilities when participants detected only one stimulus incorrectly.
**b)** Significantly increased network transition probabilities when participants correctly detected two stimuli. A graph including network 5 and 6 is depicted in supplementary figure 5.

A higher transition probability from the frontal network to the alpha-parietal and the high-beta/gamma network decreased the likelihood of correctly detecting the stimuli (Fig. 3a). In contrast, the likelihood of correct stimuli detection increased when the transition probability was higher from the alpha-parietal network to the cross-brain, the frontal, and the high-beta/gamma network, as well as from the high-beta/gamma network to the cross-brain, the frontal and the alpha-parietal network (Fig. 3b). Interestingly, the high-beta/gamma and alpha-parietal networks were the only pair with a reciprocally higher transition probability when participants correctly detected the stimuli.

## Faster network transitions improve tactile perception

Whether one or two stimuli were perceived crucially depended on the configuration of network transitions preceding them. This finding shows the importance of whole-brain network interactions for the perception of ambiguous stimuli. We now focus on three characteristics of network transitions that may differ across trials. First, we consider the rate of inter-network switching, measured by the number of network visits per second during the pre-stimulus period. Second, we assess the temporal presence of networks, both in terms of the duration of each visit (lifetime of a network) as well as the overall share of time spent in a particular network (fractional occupancy (FO)). Results are shown in Figure 4.

The lifetime of the alpha-parietal network was the highest (alpha-parietal > all other networks; p<0.001), and its lifetime did not significantly differ between correct and incorrect detections (p=0.59). For the high-beta/gamma network, the lifetime and FO were significantly lower for correct compared to incorrect detections (p<0.001). Both the cross-brain and the frontal network had a higher temporal occupation, i.e., FO was higher for correct stimuli detection (p<0.001). In addition, correct stimulus

detections were accompanied by faster overall inter-network switching as the number of network visits per second was significantly increased.

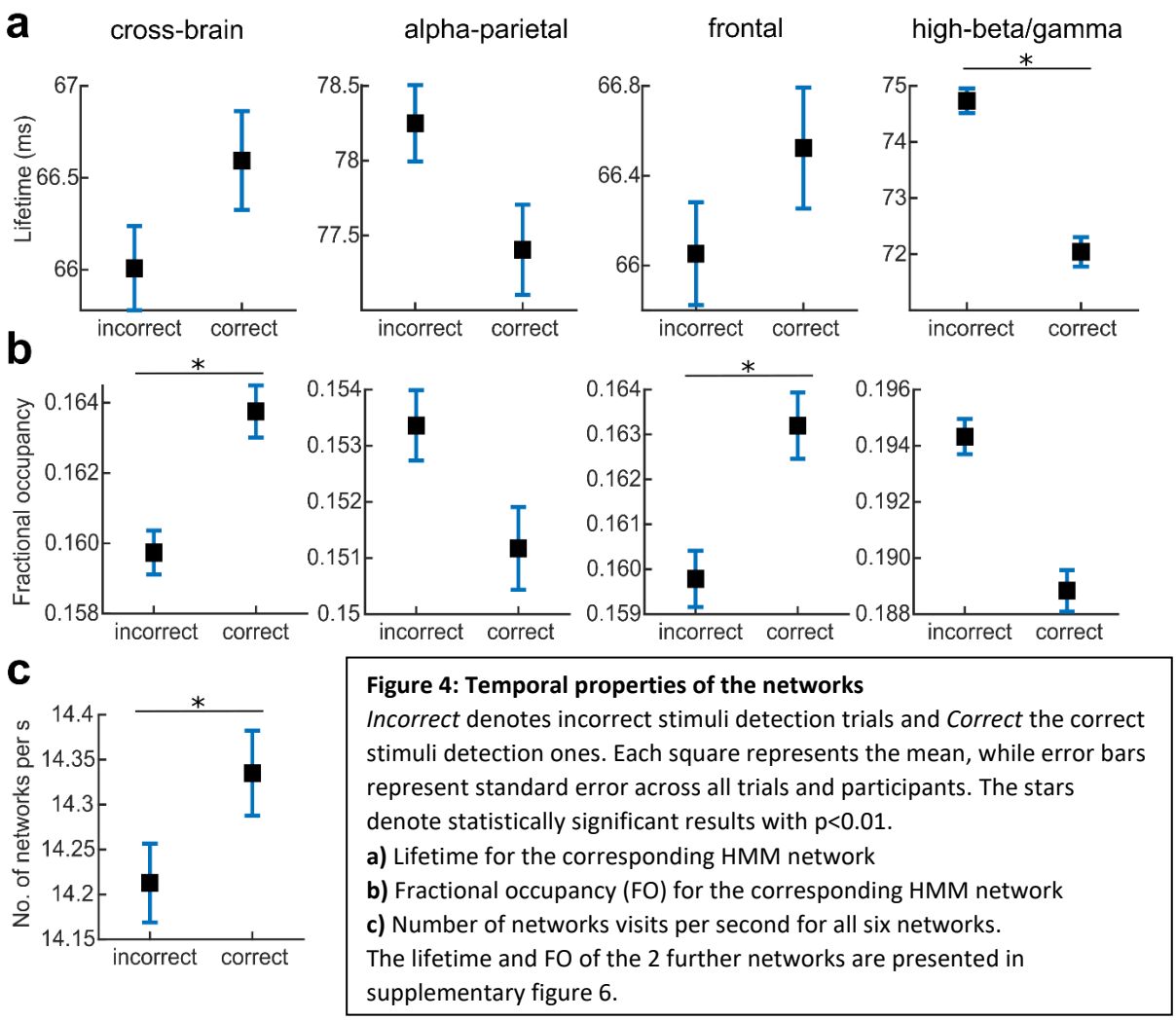


**Figure 4: Temporal properties of the networks**
*Incorrect* denotes incorrect stimuli detection trials and *Correct* the correct stimuli detection ones. Each square represents the mean, while error bars represent standard error across all trials and participants. The stars denote statistically significant results with p<0.01.
**a)** Lifetime for the corresponding HMM network
**b)** Fractional occupancy (FO) for the corresponding HMM network
**c)** Number of networks visits per second for all six networks.
The lifetime and FO of the 2 further networks are presented in supplementary figure 6.

# Discussion

Correctly detecting incoming stimuli in an uncertain, non-cued environment requires a particular dynamic pattern of pre-stimulus spontaneous brain activity. Such a pattern allows the brain to optimally integrate the incoming stimuli to reach a correct decision. In our work, we identified whole-brain networks from the pre-stimulus resting period. We identified different temporal characteristics depending on the percept: Correct detections were characterized by higher transition probabilities from the alpha-parietal and high-beta/gamma networks to the frontal network and lower probabilities to the cross-brain network. In addition, faster inter-network switching preceded correct stimulus detection, suggesting a need for higher flexibility in the brain. For correct stimuli detection, the spectrally-specific networks, i.e., the alpha-parietal and high/beta network, exhibited a higher probability of transitioning to multi-frequency networks, i.e., the cross-brain and frontal network. Our findings point to the relevance of spontaneously forming whole-brain networks and their dynamic interactions for perception. This extends previous research on near-threshold stimulus detection

beyond the relevance of the short preparatory baseline period[5,6,20–22], and thus points to the functional relevance of spontaneously forming whole-brain networks.

## Spontaneous whole-brain networks related to perception

The multi-frequency networks either distribute information (frontal network) or integrate information (cross-brain network) from different networks. To receive inputs from and send outputs to different spectrally-specific networks, the cross-brain network and the frontal network require multi-frequency coherence to synchronize incoming information across multiple frequencies. On the one hand, the cross-brain network is integrative in nature because when higher-order brain interactions are considered, the connectivity is restricted to the left and right pre-central gyri, frontal, and parietal regions. On the other hand, the frontal network is distributive because multi-frequency coherence is accompanied by a densely connected manifold. This connectivity pattern of the frontal network aligns with frontal cortical regions performing heterogeneous and complex functions via multiplexed oscillatory coding[14,23–27]. Hence, the frontal network is plausibly responsible for multiplexed oscillatory coding such that the frontal cortex modulates coupling with other brain areas. This multiplexed information transmission, in turn, makes it possible for the information to flow through the whole brain, as demonstrated by dense connections to other regions. Correct detection of stimuli was more likely when network transitions to the distributive frontal network or integrative cross-brain network had a higher probability, thus indicating the relevance of these two networks.

In the case of the high-beta/gamma network – a spectrally specific network – the left post- and precentral regions were embedded within a network of prefrontal areas. The spectral properties and the connectivity properties for the high-beta/gamma network align with previously reported findings in literature: In the sensorimotor system, beta activity is considered inhibitory[28,29], while in the prefrontal regions, beta activity tends to indicate reactivation of neuronal ensembles for further processing[30–32]. Of note is the presence of the right IP-r in the cluster of prefrontal and left sensory-motor regions. It is known that IP-r in the human brain detects salient stimuli within sequences and controls attention over time[33,34]. Hence, the high-beta/gamma network includes an ensemble of fronto-parietal cortical regions that activate perceptually relevant sensory-motor regions. Furthermore, the high-beta/gamma network is the only one with a lower lifetime during correct trials, despite showing the largest FO for both percepts. This highlights the role of duration in the action of high-beta/gamma activity in the brain.

The spectral characteristics and the connectivity of the alpha-parietal network are consistent with the modulating role of parietal alpha activity for attention[35–37]. Dense pair-wise alpha-band coherence between brain regions in the alpha-parietal network exhibited sparse connectivity dominated by parietal areas. This finding relates to the more generic role of posterior alpha activity in gating cortical processing[38–40]. Furthermore, the lifetime of the alpha-parietal network was the longest among all networks and did not significantly differ between correct and incorrect stimuli detections. Hence, we don't observe a mere omission of the alpha-parietal network for correct stimuli detections. Rather, transitions occur back and forth between the alpha-parietal network and the high-beta/gamma network, and the alpha-parietal network has a higher probability of transitioning to multi-frequency networks.

## Connectivity manifolds for network descriptions

HMM is an unsupervised method, blind to the underlying biology of the time series it is fit on. The algorithm is not explicitly built to extract physiologically interpretable features. Hence, the connection

between biology and the HMM networks is post-hoc. Spectral coherence revealed pair-wise connectivity between fronto-parietal and sensorimotor cortices, but the overlap in coherence between the identified networks complicates the interpretation of each network's physiological relevance. Hence, we used diffusion maps on network-specific covariance vectors of each brain area to capture higher-order connectivity between different brain regions within each HMM network. Diffusion maps can extract a low-dimensional representation of data while preserving similarity calculated in higher dimensions. The low-dimensional representation of the data allowed identifying a brain network's most critical connections. In our case, the cross-brain and the frontal network exhibited multi-frequency and spatially distributed spectral coherence. However, the connectivity map allowed us to disentangle the integrative role of the cross-brain network and the distributive role of the frontal network. Hence, diffusion maps offer a complementary framework to coherence-based whole-brain networks. At the same time, we cannot answer whether the connectivity observed on the manifold is responsible for producing the spectral features within the coherence-based network or vice-versa. This remains a crucial question for future work.

### Conclusion

Over the years, specific brain regions and their spectral properties have been linked to perception. However, brain areas do not operate alone but are intensely connected with each other. We here highlight that the likelihood of correctly detecting the tactile stimuli increased when it was more likely to transition from spectrally specific to multi-frequency networks. These changes in temporal network characteristics indicate that for correct stimulus detection, whole-brain networks need to be able to switch more flexibly and reconfigure network connectivity between sensorimotor, frontal, and parietal regions. Our findings collectively underscore the relevance of spontaneously forming whole-brain networks before the task for understanding mechanisms of perception.

## Acknowledgments

This work was supported by the DFG grant FL 760/4-1 awarded to Esther Florin. We want to thank Lena Spitz for her assistance in recruiting participants for the study. We would also like to thank Johannes Pfeifer for his feedback on the manuscript.

## Competing interests

None of the authors have any competing interests.

## STAR Methods

### Tactile discrimination paradigm

Thirty healthy participants (15 females and 15 males, right-handed, 26.4 (mean), 25 (median), 13 (range) years in age) volunteered to perform the task. The experimental procedure was explained to all participants. Everyone provided written consent, and the study was approved by the local ethics committee at the Medical Faculty of Heinrich Heine University, Düsseldorf (study number 2019-477) and conducted in accordance with the Declaration of Helsinki.

We adopted the tactile discrimination task described in detail in Baumgarten et al. (2016) to accommodate our network analysis. Each trial started with the presentation of a start cue (500 ms). Next, the cue decreased in brightness, indicating the pre-stimulus period (randomized to last between 10-15 seconds), after which the subjects received either one or two short (0.3 ms) electrical pulses applied by two electrodes placed between the two distal joints of the left index finger. The time between the two pulses (Stimulus Onset Asynchrony (SOA)) was determined with a staircase procedure for each participant prior to the main experiment so that they had a hit rate of 50%. This SOA is termed the *critical SOA* (crit SOA). Participants had to respond to whether they perceived one or two stimuli with their right hand by pressing a button with either their right index or middle finger. The index and middle finger options were randomly swapped at each trial. SOAs were varied in a pseudorandom manner between: 0ms, crit SOA, crit SOA + 10ms, crit SOA – 10ms, and 3 times crit SOA. The 0 and 3 times crit SOA trials were used to prevent biased responses and to be able to confirm that the participants were properly performing the task. Participants were recorded on two days: Day one for each participant started with a pre-task eyes open resting state MEG recording for 10 minutes. It continued with the stair-case procedure and the MEG data recordings during the task. The task was divided into four blocks per day of about 45-50 trials. Each block lasted about 10-15 minutes. Participants were allowed to take breaks between blocks. Finally, a 10-minute post-task eyes-open resting state recording was performed.

On day two, the staircase procedure was repeated. This was followed by four measurement blocks of tasks during which MEG data were recorded. In total, across the two days, 200 trials with crit SOA, 50 of the other four conditions were acquired per participant. On the first day, crit SOA across subjects was 71ms (mean) +- 34.3ms (standard deviation); on the second day, crit SOA across subjects was 79.8ms (mean) +- 34.0 ms (standard deviation). The overall average crit SOA was 75ms (mean) +- 34.0 ms (standard deviation). The accuracy across different SOAs is shown in supplementary figure 7.

## Electrophysiological recording

MEG data were recorded on both days of task performance. We used a whole-head MEG system with 306 channels (Elekta Vectorview, Elekta Neuromag, Finland) housed within a magnetically shielded chamber. Electrooculography and electrocardiography were recorded simultaneously with MEG data to be later able to remove eye blink and cardiac artifacts. Data were acquired at a sampling rate of 2500Hz with an 833Hz low pass filter.

## Pre-processing

All data processing and analyses were performed using Matlab (version R 2021b; MathWorks, Natick, MA) and the Brainstorm toolbox[41]. The Neuromag system provides signal-space projection (SSP) vectors for cleaning environment noise from the MEG channels, which were applied. The line noise was removed from all channels with a notch filter at 50, 100, 150, ..., 550, and 600 Hz with a 3 dB bandwidth of 1 Hz. To ensure artifact-free data, we visually inspected the data. Very noisy and flat MEG channels were excluded from further analysis. Time segments containing artifacts were marked in the time series. However, if artifacts regularly occurred only in one channel, this whole channel was removed. Frequently arising artifacts following the same basic pattern, such as eye blinks or cardiac artifacts, were removed via SSP using projectors that were calculated separately for the cardiac and blink artifacts. All data were high-pass filtered with 1 Hz to remove movement-related low-frequency artifacts. Finally, the data were downsampled to 1000 Hz. All trials with artifacts were excluded from further analysis. For each trial, we extracted pre-stimulus activity that ranged from -8.0 seconds to -0.1 seconds, with 0 indicating the onset of the electric stimuli. This time window was chosen as it

effectively excludes any post-response or pre-stimulus activity. Each channel's data were mean corrected by the average across the trial (-8.0s to -0.1s).

Cortically constrained source estimation was performed on these data at the participant level using each participant's anatomy. Using FreeSurfer (https://surfer.nmr.mgh.harvard.edu/, v.5.3.0), the participants' cortical surfaces were extracted from the individually acquired T1-weighted MRI scans (3T scanner and 1 $mm^3$ voxel size). The MRI was acquired after both MEG sessions had been recorded. We used the overlapping spheres method[42] with 306 spheres for the forward model and a linearly constrained minimum variance (LCMV) beamformer as the inverse model. The data covariance matrix for the LCMV beamformer was computed per measurement block of each participant, and the matrix was regularized by setting the values below the median to the median eigenvalue of the data covariance matrix. The noise covariance was obtained from a five-minute empty room recording on the same day as the measurement. A single shared source kernel was obtained for each measurement block of every participant.

For every trial and each participant, the source-reconstructed MEG data were projected to the default cortical anatomy (MNI 152 with 15,002 vertices) using registered spheres extracted using FreeSurfer and MRIs of individual participants[43] and then down-sampled to 250 Hz. We used the Mindboggle atlas[44] to spatially reduce the data dimensions. For each of the 42 cortical regions in the atlas, for every trial, we obtained the first principal component from the vertices' time series within that region. To correct for volume conduction in the signal, symmetric orthogonalization[45] was applied to these PCA (principal component analysis) time series. This resulted in 42 multivariate time series for each trial and each participant. The row vectors of this orthogonalized matrix, obtained for every trial, were z-scored. The entire pre-processing pipeline described in this paragraph was applied to all trials of every participant, irrespective of the response type on a trial.

Finally, to resolve sign ambiguity inherent in source-reconstructed MEG data across participants, a sign-flip correction procedure[46] was applied to the entire dataset, i.e., across all trials and participants. Subsequently, this dataset was then fed to the TDE-HMM pipeline described in the next section.

## TDE-HMM pipeline

The HMM is a data-driven probabilistic algorithm that finds recurrent network patterns in a multivariate time series[12,47]. Each network pattern is referred to as a 'state' in the HMM framework, such that these networks can activate or deactivate at various points in time. We use network throughout the text when referring to an HMM state. We used a specific variety of the HMM, the time delay embedded (TDE)-HMM, where whole-brain networks are defined in terms of spectral power and phase coupling[10]. For every point in time, the HMM algorithm provides the probability that a network is active. In our approach, we also performed spectral analyses of these networks, leading to a complete spatio-spectral connectivity profile across the cortex. A summary of the MEG data processing is provided in supplementary figure 8.

## HMM model fitting

Since we were interested in recovering phase-related networks, the TDE-HMM was fit directly on the time series obtained after the pre-processing steps described in the previous section, as opposed to its power envelope. This preserved the cross-covariance within and across the underlying time series of the cortical regions.

The HMM-MAR toolbox[46] was used for fitting the TDE-HMM. We opted for six different networks as a reasonable trade-off between the spectral quality of the results and their redundancy. The embedding took place separately in a 60 ms window (i.e., a 15-time point window for a sampling frequency of 250 Hz) for each trial. Since time embedding increases the number of rows of the data from 42 to 42 times the number of window samples, an additional PCA step was performed along the spatial dimension. The number of components retained was 84 (42 times 2) following our previous pipeline[47] and as recommended in reference 11. A full covariance matrix with an inverse Wishart prior was used to characterize each network. The network transition matrix of an HMM is described by a two-dimensional multinomial distribution. The conjugate prior for a two-dimensional multinomial distribution is a two-dimensional Dirichlet distribution. A two-dimensional Dirichlet distribution can be parameterized by concentration parameters alpha. The diagonal alphas were set to 10, and the off-diagonal were set to 1. The 'zero mean' option in the HMM toolbox was chosen to ensure that the mean of the time series did not take part in driving the networks. We used the stochastic version of variational inference for the HMM to speed up the fitting process. The 'HMM-MAR'-type initialization was used to start the optimization process (for details, see ref.[46]). A single HMM was fit across all participants and trials where the SOA was in the range critical SOA +- 10ms, irrespective of correct or incorrect stimuli detection. We hypothesized that correct and incorrect detections involve the same spontaneous networks, but their temporal interactions differ in the pre-stimulus epochs, leading to different detections.

## Data-driven frequency bands

We investigated the spectral connectivity patterns across the different networks. The objective was to uncover significant coherence within frequency bands in the respective networks. The HMM output includes a multidimensional "gamma" time series containing the probability for each network at a given point in time. A network was considered to be active at a given time point if the gamma value for that specific network was greater than or equal to 0.85. A contiguous block of time for which the gamma value for a specific network remains higher than 0.85 is referred to as a 'network visit'. These network time courses allowed the extraction of network-specific data for each trial for further analysis. For each HMM network, we filtered the network-specific data for all trials between 1 and 45 Hz. Then, we calculated the Fourier transform of the data using a multi-taper approach to extract the frequency components from the short segments of each network visit[10]. Seven Slepian tapers with a time-bandwidth product of 4 were used, resulting in a frequency resolution of 0.5 Hz. Subsequently, we calculated the coherence and power spectral density of these binned frequency domain data separately for every network within each trial. For each trial, the coherence and the power spectral density obtained were three-dimensional matrices of size f (number of frequency bins) by N (42 cortical locations) by N. We call these trial-level coherence matrices.

Based on the trial-level coherence matrices, we performed a frequency band-specific analysis. The lower triangular portion of the trial-level coherence matrix obtained above was vectorized across columns for each subject and all their trials. This resulted in 903 (lower triangular entries of a 42 by 42 matrix including the diagonal) by f (number of frequency bins) matrices for each trial. Subsequently, we averaged all matrices across trials and participants along the spectral dimension (number of frequency bins), resulting in a single 903 by f matrix per network. This procedure was repeated for all six networks. Finally, we concatenated matrices across all networks, resulting in a group-level coherence matrix (f by 903 by 6). We factorized the group-level coherence matrix into four frequency modes using a non-negative matrix factorization (NNMF)[48]. In contrast to the traditional definition of frequency bands in electrophysiological data, i.e., delta, theta, alpha, beta, and gamma, these

frequency modes are data-driven descriptions of the spectral space and were obtained from non-negative matrix factorization of the Fourier-transformed data[10]. Canonical definitions of frequency bands assign equal weight to each frequency bin within a band for every subject, which might not be suitable for analyses across a large dataset.

The frequency mode weights are the NNMF weights obtained from the NNMF estimation (which, just like a regression coefficient, are unitless because coherence is unitless) (see supplementary figure 1). Three modes mostly correspond to the canonical alpha, beta, and high beta/gamma band, whereas the fourth represented the 1/f noise in neural signals. Since NNMF does not guarantee a unique solution, we performed multiple instances of the factorization. In practice, we could obtain frequency modes corresponding to the classical frequency bands within four algorithm iterations. At each instance, we visualized the output to ensure the frequency specificity of the frequency modes. The output stability was ensured using 'robust NNMF', a variant of the NNMF algorithm[10]. We then computed the inner product between the trial-and group level coherence matrix and the frequency modes obtained above. We called these the trial-level and group-level coherence projections, respectively. While these frequency modes were derived from coherence, they can be applied to power measures or any other frequency-specific measure. We used these factors to calculate the power spectra for each of the 42 regions and to obtain trial-level and group-level power projections.

## Group-level coherence ring figures

To separate background noise from the most robust coherent connections, a Gaussian mixture model (GMM) was used[10]. For the group-level coherence projections, we normalized the activity in each network for each spectral band by subtracting the mean coherence within each frequency mode across all networks. As a prior for the mixture model, we used two single-dimensional Gaussian distributions with unit variance: one mixture component to capture noise and the other to capture the significant connections. This GMM with two mixtures was applied to the coherence values of each network. Connections were considered significant if their p-value after correction for multiple comparisons (Bonferroni correction) was smaller than 0.001.

## Power spectral density test

We used permutation testing to assess power increases within a brain region relative to others within a network. For this, we used trial-level power projections. We subtracted the mean power across all networks and all trials from each of the 42 regions within a network for each trial. We then permuted the labels for the 42 brain regions within a network across trials to obtain a null distribution. The p-value was calculated as the number of permutations for which the power of a specific brain region was higher or lower than the shuffled set divided by the total number of permutations. We used 5000 permutations to compute our results.

## Diffusion map analysis

We used diffusion maps to recover a low-dimensional network embedding from high-dimensional cortical data[15,49]. The objective of the diffusion maps algorithm is to uncover the underlying structure of high-dimensional data, in this case, multivariate brain data. The following steps were performed to calculate network-specific embeddings: We masked the original dataset, i.e., the one without any delay embedding, using the network probability time course (HMM gamma output). The probability threshold for gamma was the same 0.85 as used to perform the multi-taper spectral analysis. The network time courses allowed the extraction of network-specific data for each trial for further

analysis. Using the network-specific data, we computed a network-specific covariance matrix. The covariance matrix was then used to perform diffusion map analysis.

The diffusion map algorithm can be broken down into four main steps:

1. Define a similarity measure between pairs of data points
2. Construct a graph using the similarity measure
3. Compute the transition matrix and perform a diffusion process
4. Calculate the diffusion coordinates for a low-dimensional embedding

Step 1: Similarity measure

The similarity measure used in diffusion maps is typically a function that measures the distance between two data points. Let **C** be the covariance matrix for all brain regions, where **C (i, j)** represents the covariance between regions **i** and **j**.

To calculate the similarity between regions **i** and **j** based on the covariance matrix, we can use the following steps:

**C (i, :)** and **C (j, :)** are covariance vectors, i.e., the rows of the covariance matrix corresponding to regions **i** and **j**, respectively.

The similarity measure between **i** and **j** is defined as the Spearman rank correlation $\rho\big(C(i,:), C(j,:)\big)$

Then we can define a similarity matrix:

$$W(i,j) = \rho\big(C(i,:), C(j,:)\big)$$

Step 2: Graph construction

Using the similarity measure, we can construct a weighted graph G = (V, E) where V is the set of brain regions and E is the set of edges between brain regions. The weight of an edge between two brain regions i and j is given by the similarity measure calculated previously.

$$w_{ij} = W(i,j)$$

This similarity measure can be said to capture higher-order relationships between regions i and j that play an important role in complex systems such as the brain[17–19].

Step 3: Diffusion process

To perform the diffusion process, we compute the diffusion operator $P_\alpha$, which is defined as:

$P_\alpha = {D_\alpha}^{-1} W_\alpha$**.** Here, $\alpha \in [0,1]$ is the diffusion parameter used by the diffusion operator. The parameter α was set to 0.5 as per previous recommendation for large-scale brain data[16,50,51]. $W_\alpha$ and $D_\alpha$ are defined as follows:

$$W_\alpha = D^{-1/\alpha} W D^{-1/\alpha}$$

$$D(i,i) = \sum_j W(i,j), \text{ with the off-diagonal elements set to 0}$$

$$D_\alpha = \sum_j W_\alpha(i,j).$$

D is the degree matrix of the graph derived from W. Once $P_\alpha$ has been calculated, we can run the diffusion process multiple times by taking larger powers of $P_\alpha$, i.e., $P_\alpha^t$ , where t is called the time or

the scale parameter[49]. We ran a single-step diffusion process with t=1. This was in line with the previous usage of diffusion maps for large-scale brain datasets[16,50,51].

Step 4: Diffusion coordinates and low-dimensional embedding

Once $P^1_{0.5}$ has been calculated, we can perform a generalized eigenvalue decomposition of the $P^1_{0.5}$ matrix.

$$P^1_{0.5(i,j)} = \sum_l \lambda^1_l \psi_l(x_i)\phi_l(x_j)$$

where $\{\lambda^1_l\}$ is the sequence of eigenvalues of $P^1_{0.5}$. $\{\psi_l\}$ and $\{\phi_l\}$ are the right and left eigenvectors, respectively.

Finally, the diffusion map can be defined as the new set of coordinates for the data that we can find using the right eigenvectors.

$$\psi_1(x) = \left(\lambda^1_1\psi_1(x), \lambda^1_2\psi_2(x), \dots \lambda^1_k\psi_k(x)\right)$$

Using $\psi_1(x)$ we can embed the data into an Euclidean space, which we term as the connectivity manifold in our results. For a complete theoretical description of diffusion maps, please refer to reference[48].

The dimensionality was reduced from 42 to 5. Only the top three dimensions were used for subsequent analysis by looking at the elbow of the scree plot. The top three dimensions captured 75% of the variance in the data. The above procedure was implemented using custom-written scripts and Brainspace toolbox[52].

## Statistical testing on the connectivity manifold

The connectivity manifold indicates the distance between different brain regions. In short, the smaller the distance between two regions on the manifold, the stronger the connectivity between the two regions (direct and indirect combined). For details about the relationship between distance and connectivity, please refer to Methods: Diffusion map analysis. To test if certain brain regions showed significant connectivity on the manifold, we applied the same test described in Methods: Group level coherence ring figures.

## Transition matrix test

We estimated transition matrices for each trial. For every trial, a transition matrix contains probabilities for different HMM networks to switch to and from one another. Non-parametric permutation testing (5000 permutations) was performed to compare network transitions between correct and incorrect trials. Results were considered significant if $p<0.01$ after correction for multiple comparisons using the Benjamini Hochberg FDR correction[53].

## Temporal properties

To test for changes in the temporal properties for percept one versus percept two stimuli, we compared the lifetimes and FO for each network within and across the response types using two-way repeated measures ANOVA followed by post-hoc tests. A network's lifetime for a given visit refers to the time spent in that network. Of note, the lifetime of a network can be shorter than one oscillation cycle because the frequency is the rate of change of a signal, and this rate can be estimated by examining the slope of the signal at any instant in time[10]. FO is defined as the average share of time

spent in a particular network. Finally, we assessed the overall network changes per second rate is defined as the number of times one network switches to another per second.

# References


1. Romo, R. & Rossi-Pool, R. Turning Touch into Perception. *Neuron* **105**, 16–33 (2020).
2. Linkenkaer-Hansen, K., Nikulin, V. V., Palva, S., Ilmoniemi, R. J. & Palva, J. M. Prestimulus sscillations enhance psychophysical performance in humans. *J. Neurosci.* **24**, 10186–10190 (2004).
3. Rajagovindan, R. & Ding, M. From prestimulus alpha oscillation to visual-evoked response: an inverted-U function and its attentional modulation. *J. Cogn. Neurosci.* **23**, 1379–1394 (2011).
4. Iemi, L. *et al.* Multiple mechanisms link prestimulus neural oscillations to sensory responses. *eLife* **8**, e43620 (2019).
5. Baumgarten, T. J., Schnitzler, A. & Lange, J. Prestimulus alpha power influences tactile temporal perceptual discrimination and confidence in decisions. *Cereb. Cortex N. Y. N 1991* **26**, 891–903 (2016).
6. Podvalny, E., Flounders, M. W., King, L. E., Holroyd, T. & He, B. J. A dual role of prestimulus spontaneous neural activity in visual object recognition. *Nat. Commun.* **10**, 3910 (2019).
7. Rassi, E., Wutz, A., Müller-Voggel, N. & Weisz, N. Prestimulus feedback connectivity biases the content of visual experiences. *Proc. Natl. Acad. Sci. U. S. A.* **116**, 16056–16061 (2019).
8. Li, Y., Ward, M. J., Richardson, R. M., G'Sell, M. & Ghuman, A. S. Endogenous activity modulates stimulus and circuit-specific neural tuning and predicts perceptual behavior. *Nat. Commun.* **11**, 4014 (2020).
9. Thiebaut de Schotten, M. & Forkel, S. J. The emergent properties of the connected brain. *Science* **378**, 505–510 (2022).
10. Vidaurre, D. *et al.* Spontaneous cortical activity transiently organises into frequency specific phase-coupling networks. *Nat. Commun.* **9**, 2987 (2018).
11. Baker, A. P. *et al.* Fast transient networks in spontaneous human brain activity. *eLife* **3**, e01867 (2014).
12. Vidaurre, D. *et al.* Discovering dynamic brain networks from big data in rest and task. *NeuroImage* **180**, 646–656 (2018).
13. Akam, T. & Kullmann, D. M. Oscillations and filtering networks support flexible routing of information. *Neuron* **67**, 308–320 (2010).
14. Akam, T. & Kullmann, D. M. Oscillatory multiplexing of population codes for selective communication in the mammalian brain. *Nat. Rev. Neurosci.* **15**, 111–122 (2014).
15. Lian, W., Talmon, R., Zaveri, H., Carin, L. & Coifman, R. Multivariate time-series analysis and diffusion maps. *Signal Process.* **116**, 13–28 (2015).
16. Margulies, D. S. *et al.* Situating the default-mode network along a principal gradient of macroscale cortical organization. *Proc. Natl. Acad. Sci. U. S. A.* **113**, 12574–12579 (2016).

17. Battiston, F. *et al.* The physics of higher-order interactions in complex systems. *Nat. Phys.* **17**, 1093–1098 (2021).

18. Busch, E. L. *et al.* Multi-view manifold learning of human brain-state trajectories. *Nat. Comput. Sci.* **3**, 240–253 (2023).

19. Santoro, A., Battiston, F., Petri, G. & Amico, E. Higher-order organization of multivariate time series. *Nat. Phys.* **19**, 221–229 (2023).

20. Baumgarten, T. J., Schnitzler, A. & Lange, J. Beta oscillations define discrete perceptual cycles in the somatosensory domain. *Proc. Natl. Acad. Sci. U. S. A.* **112**, 12187–12192 (2015).

21. Florin, E., Vuvan, D., Peretz, I. & Baillet, S. Pre-target neural oscillations predict variability in the detection of small pitch changes. *PloS One* **12**, e0177836 (2017).

22. Busch, N. A., Dubois, J. & VanRullen, R. The phase of ongoing EEG oscillations predicts visual perception. *J. Neurosci.* **29**, 7869–7876 (2009).

23. Benchenane, K., Tiesinga, P. H. & Battaglia, F. P. Oscillations in the prefrontal cortex: a gateway to memory and attention. *Curr. Opin. Neurobiol.* **21**, 475–485 (2011).

24. Buschman, T. J., Denovellis, E. L., Diogo, C., Bullock, D. & Miller, E. K. Synchronous oscillatory neural ensembles for rules in the prefrontal cortex. *Neuron* **76**, 838–846 (2012).

25. Voytek, B. *et al.* Oscillatory dynamics coordinating human frontal networks in support of goal maintenance. *Nat. Neurosci.* **18**, 1318–1324 (2015).

26. Helfrich, R. F. & Knight, R. T. Oscillatory dynamics of prefrontal cognitive control. *Trends Cogn. Sci.* **20**, 916–930 (2016).

27. Naud, R. & Sprekeler, H. Sparse bursts optimize information transmission in a multiplexed neural code. *Proc. Natl. Acad. Sci. U. S. A.* **115**, E6329–E6338 (2018).

28. Donner, T. H., Siegel, M., Fries, P. & Engel, A. K. Buildup of choice-predictive activity in human motor cortex during perceptual decision making. *Curr. Biol.* **19**, 1581–1585 (2009).

29. Pogosyan, A., Gaynor, L. D., Eusebio, A. & Brown, P. Boosting cortical activity at beta-band frequencies slows movement in humans. *Curr. Biol.* **19**, 1637–1641 (2009).

30. Haegens, S. *et al.* Beta oscillations in the monkey sensorimotor network reflect somatosensory decision making. *Proc. Natl. Acad. Sci.* **108**, 10708–10713 (2011).

31. Miller, E. K., Lundqvist, M. & Bastos, A. M. Working Memory 2.0. *Neuron* **100**, 463–475 (2018).

32. Spitzer, B. & Haegens, S. Beyond the status quo: A role for beta oscillations in endogenous content (re)activation. *eNeuro* **4**, ENEURO.0170-17.2017 (2017).

33. Royal, I. *et al.* Activation in the right inferior parietal lobule reflects the representation of musical structure beyond simple pitch discrimination. *PloS One* **11**, e0155291 (2016).

34. Singh-Curry, V. & Husain, M. The functional role of the inferior parietal lobe in the dorsal and ventral stream dichotomy. *Neuropsychologia* **47**, 1434–1448 (2009).

35. Klimesch, W. α-band oscillations, attention, and controlled access to stored information. *Trends Cogn. Sci.* **16**, 606–617 (2012).

36. Vollebregt, M. A., Zumer, J. M., Ter Huurne, N., Buitelaar, J. K. & Jensen, O. Posterior alpha oscillations reflect attentional problems in boys with Attention Deficit Hyperactivity Disorder. *Clin. Neurophysiol. Off. J. Int. Fed. Clin. Neurophysiol.* **127**, 2182–2191 (2016).

37. Helfrich, R. F., Huang, M., Wilson, G. & Knight, R. T. Prefrontal cortex modulates posterior alpha oscillations during top-down guided visual perception. *Proc. Natl. Acad. Sci. U. S. A.* **114**, 9457–9462 (2017).

38. Jensen, O. & Mazaheri, A. Shaping functional architecture by oscillatory alpha activity: gating by inhibition. *Front. Hum. Neurosci.* **4**, 186 (2010).

39. Foxe, J. J. & Snyder, A. C. The role of alpha-band brain oscillations as a sensory suppression mechanism during selective attention. *Front. Psychol.* **2**, 154 (2011).

40. Zhou, Y. J., Iemi, L., Schoffelen, J.-M., Lange, F. P. de & Haegens, S. Alpha oscillations shape sensory representation and perceptual sensitivity. *J. Neurosci.* **41**, 9581–9592 (2021).

41. Tadel, F., Baillet, S., Mosher, J. C., Pantazis, D. & Leahy, R. M. Brainstorm: A user-friendly application for MEG/EEG analysis. *Comput. Intell. Neurosci.* **2011**, 879716 (2011).

42. Huang, M. X., Mosher, J. C. & Leahy, R. M. A sensor-weighted overlapping-sphere head model and exhaustive head model comparison for MEG. *Phys. Med. Biol.* **44**, 423–440 (1999).

43. Reuter, M., Schmansky, N. J., Rosas, H. D. & Fischl, B. Within-subject template estimation for unbiased longitudinal image analysis. *NeuroImage* **61**, 1402–1418 (2012).

44. Klein, A. *et al.* Mindboggling morphometry of human brains. *PLoS Comput. Biol.* **13**, e1005350 (2017).

45. Colclough, G. L., Brookes, M. J., Smith, S. M. & Woolrich, M. W. A symmetric multivariate leakage correction for MEG connectomes. *NeuroImage* **117**, 439–448 (2015).

46. Vidaurre, D. *et al.* Spectrally resolved fast transient brain states in electrophysiological data. *Neuroimage* **126**, 81–95 (2016).

47. Sharma, A., Vidaurre, D., Vesper, J., Schnitzler, A. & Florin, E. Differential dopaminergic modulation of spontaneous cortico–subthalamic activity in Parkinson's disease. *eLife* **10**, e66057 (2021).

48. Lee, D. D. & Seung, H. S. Learning the parts of objects by non-negative matrix factorization. *Nature* **401**, 788–791 (1999).

49. Coifman, R. R. *et al.* Geometric diffusions as a tool for harmonic analysis and structure definition of data: Diffusion maps. *Proc. Natl. Acad. Sci.* **102**, 7426–7431 (2005).

50. Larivière, S. *et al.* Multiscale structure–function gradients in the neonatal connectome. *Cereb. Cortex* **30**, 47–58 (2020).

51. Vos de Wael, R. *et al.* Anatomical and microstructural determinants of hippocampal subfield functional connectome embedding. *Proc. Natl. Acad. Sci. U. S. A.* **115**, 10154–10159 (2018).

52. Vos de Wael, R. *et al.* BrainSpace: a toolbox for the analysis of macroscale gradients in neuroimaging and connectomics datasets. *Commun. Biol.* **3**, 103 (2020).

53. Benjamini, Y. & Hochberg, Y. Controlling the false discovery rate: A practical and powerful approach to multiple testing. *J. R. Stat. Soc. Ser. B Methodol.* **57**, 289–300 (1995).

# Supplementary figures

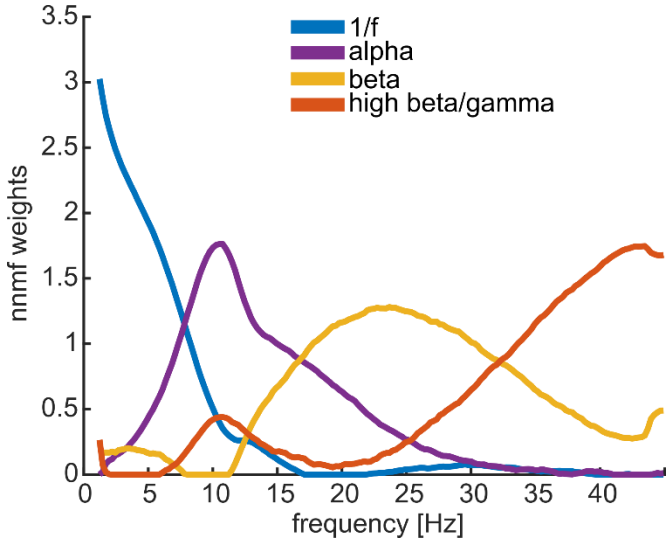


**Supplementary figure 1: Data-driven frequency bands, referred to as frequency modes in the text.** The x-axis represents frequency in Hz and the y-axis represents the weights obtained from the non-negative matrix factorisation (NNMF) in arbitrary units. The frequency resolution of the modes is 0.5 Hz (see Methods: Data-driven frequency bands).

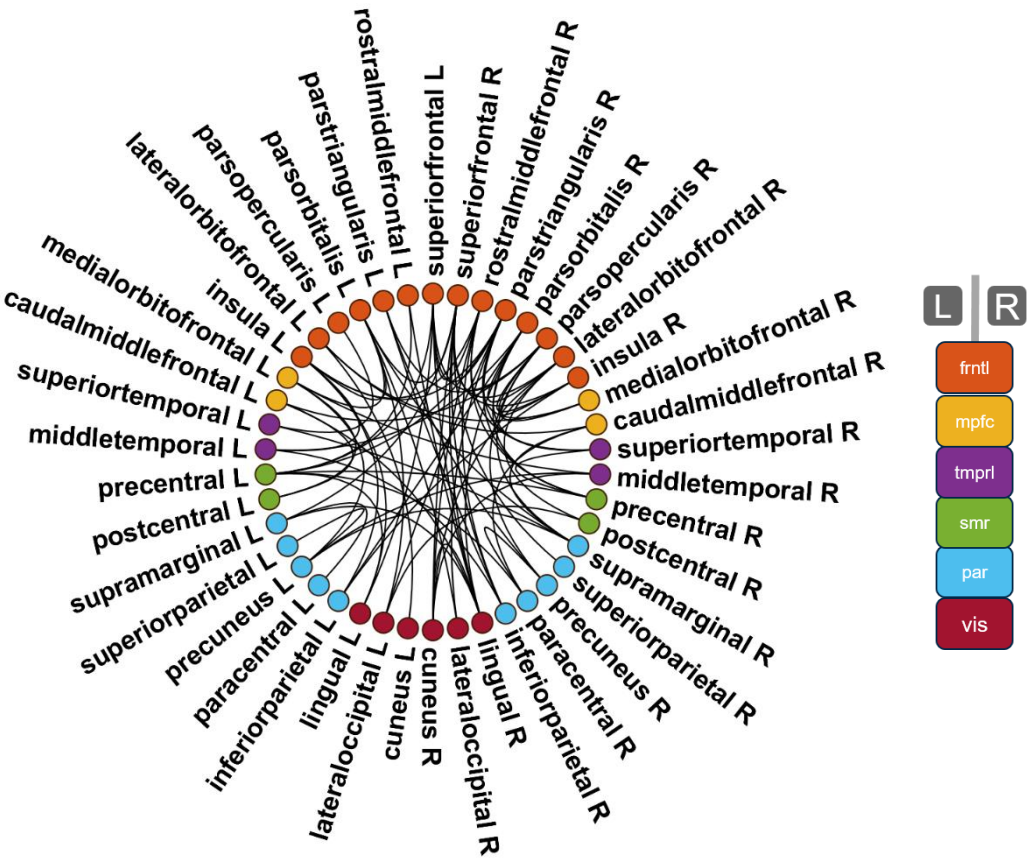


**Supplementary figure 2: Brain region labels for the ring figures.** The brain regions are based on the Mindboggle atlas.

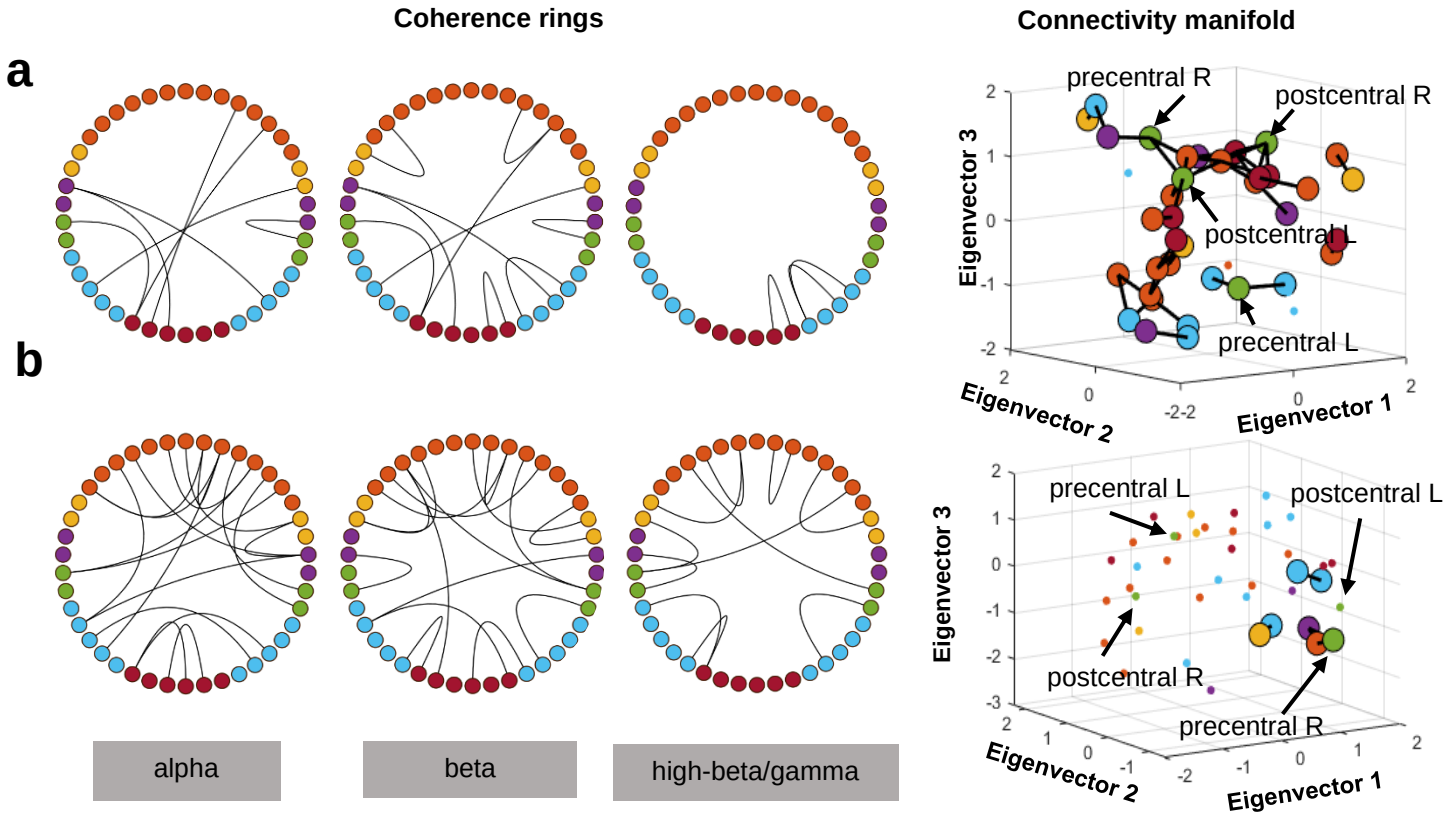


**Supplementary figure 3: Networks 5 (a) and 6 (b).**
For details on the legend see main figure 2.

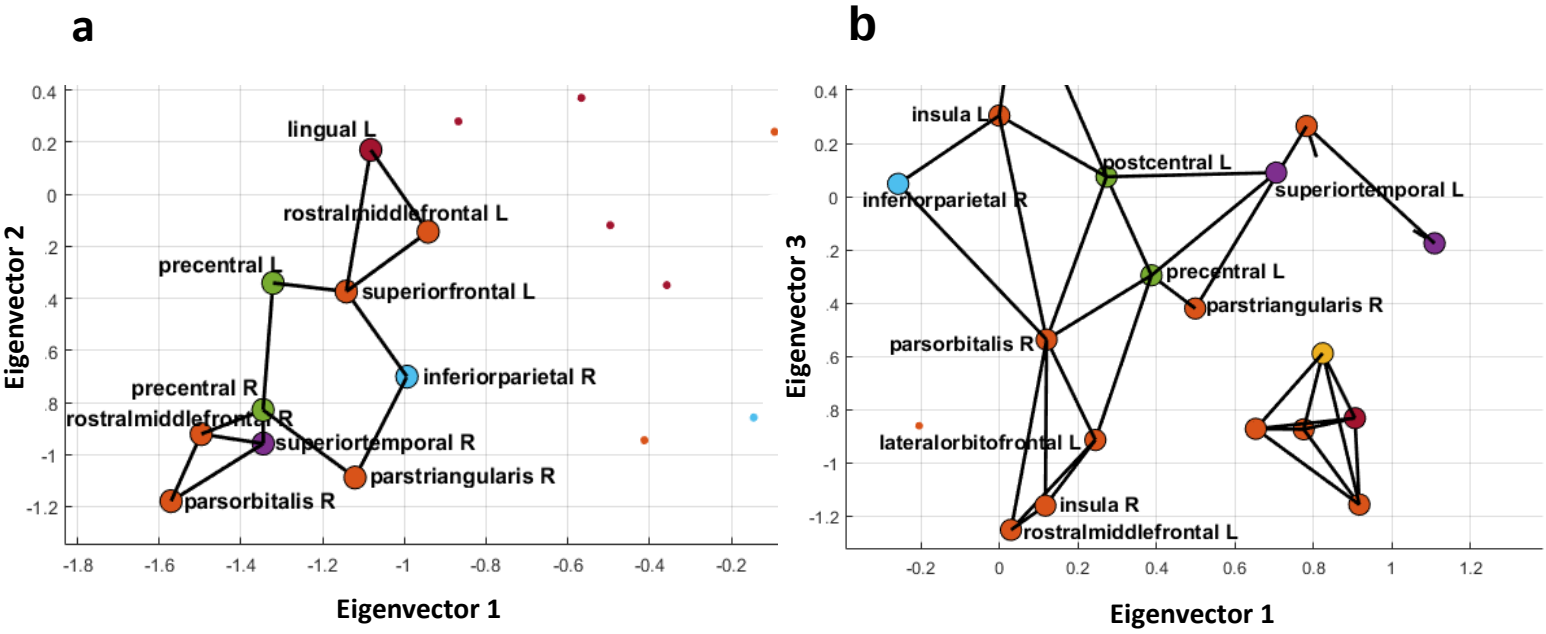


**Supplementary figure 4: Zoomed version of the connectivity manifold**. **a)** Cross-brain network **b)** High-beta/gamma network. In both the figures the inferior parietal R is connected to sensory motor regions via two frontal areas.

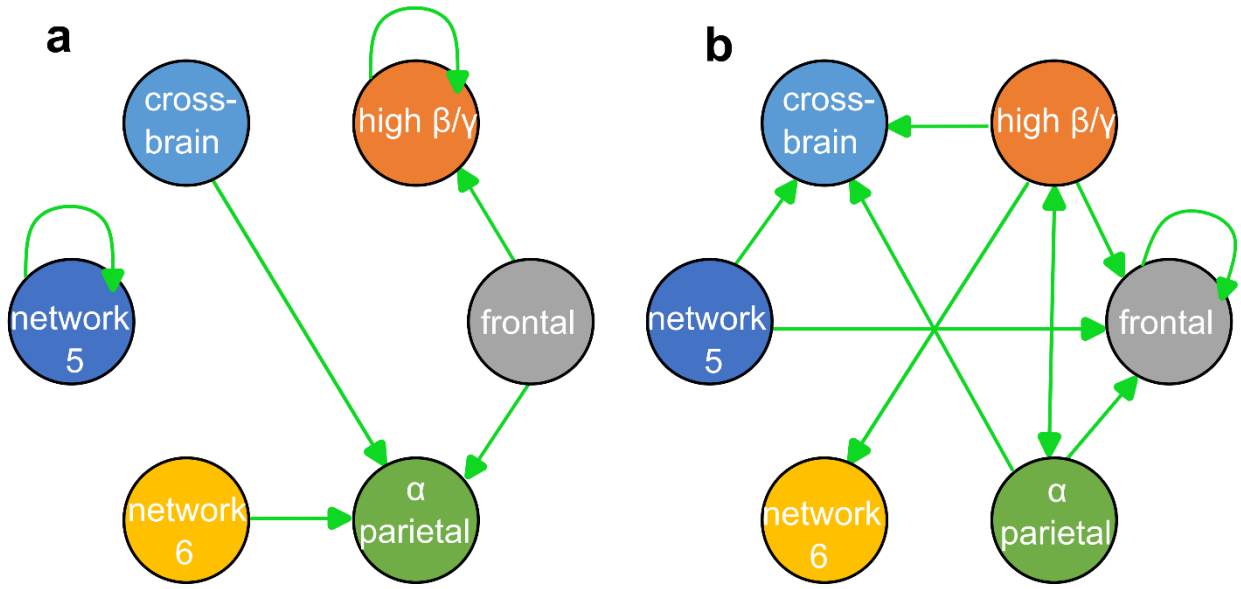


**Supplementary figure 5: Complete set of network transitions**. **a)** Significantly increased network transition probabilities when participants incorrectly detected the stimuli. **b)** Significantly increased network transition probabilities when participants correctly detected the stimuli, $p<0.05$. Not depicted transitions were statistically equally likely across perceptions.

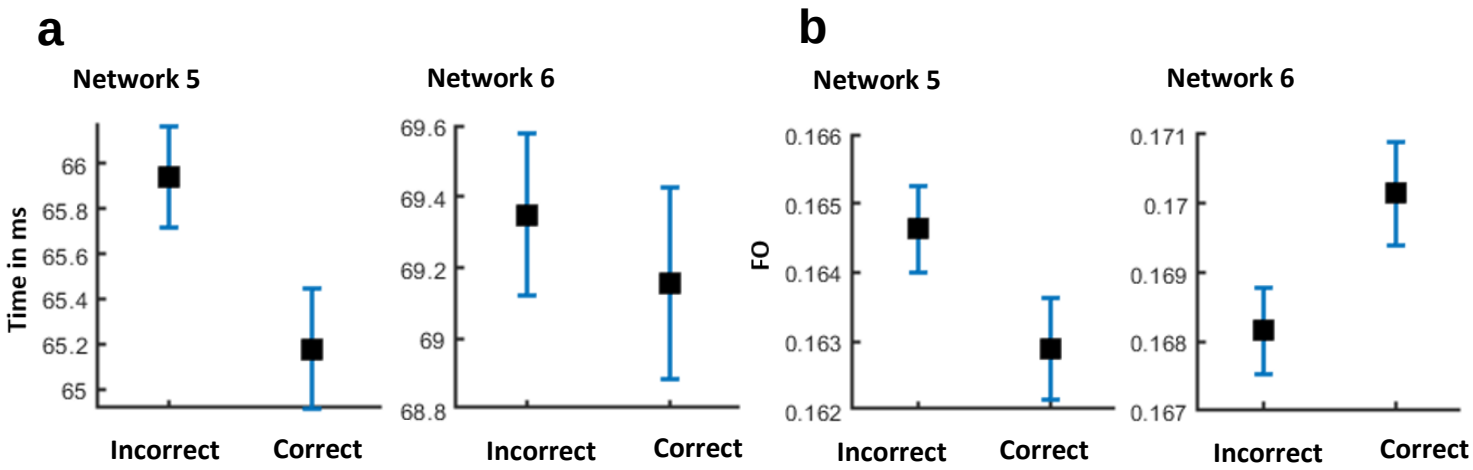


**Supplementary figure 6: Temporal properties of networks 5 and 6.**
**a)** Lifetime **b)** Fractional occupancy (FO)

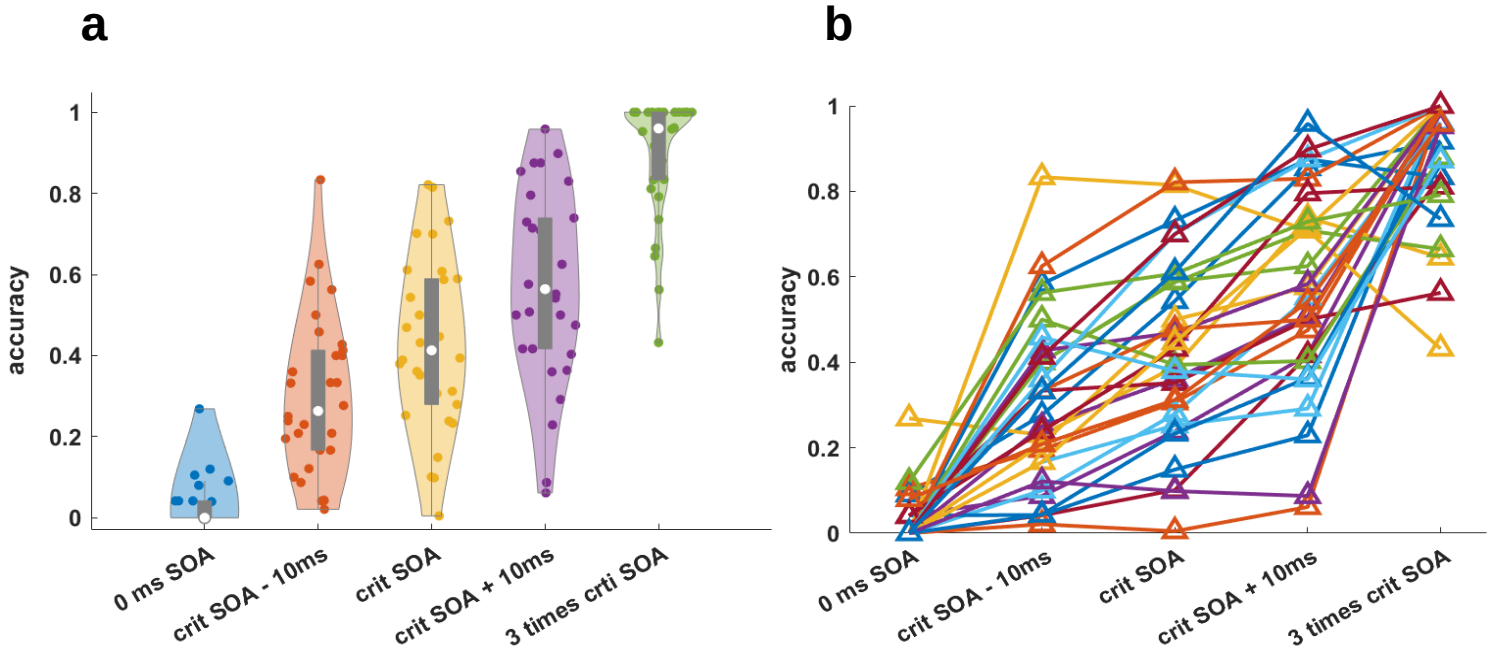


**Supplementary figure 7: Accuracy plots.**
Accuracy plot under different SOA (stimulus onset asynchrony) conditions. crit SOA: critical SOA. Accuracy was calculated per subject and per SOA condition. Accuracy was calculated by dividing the number of trials for which participants detected two electric pulses by the total number of trials.
**a)** Each violin plot includes a boxplot (grey). Box edges are formed by the first 25th percentile quartile to third 75th percentile quartile. White dots are the medians. Data minima/maxima control the whisker length. Individual scatter points within a violin plot are individual participant accuracies in a specific SOA condition. The width of each violin plot provides a probability density estimate for the accuracy given the participant data.
**b)** Individual participant accuracy plots under different SOA (stimulus onset asynchrony) conditions. Each triangle represents an individual participant's accuracy under an SOA condition. For a given participant, triangles under different SOA conditions are connected using a line plot.

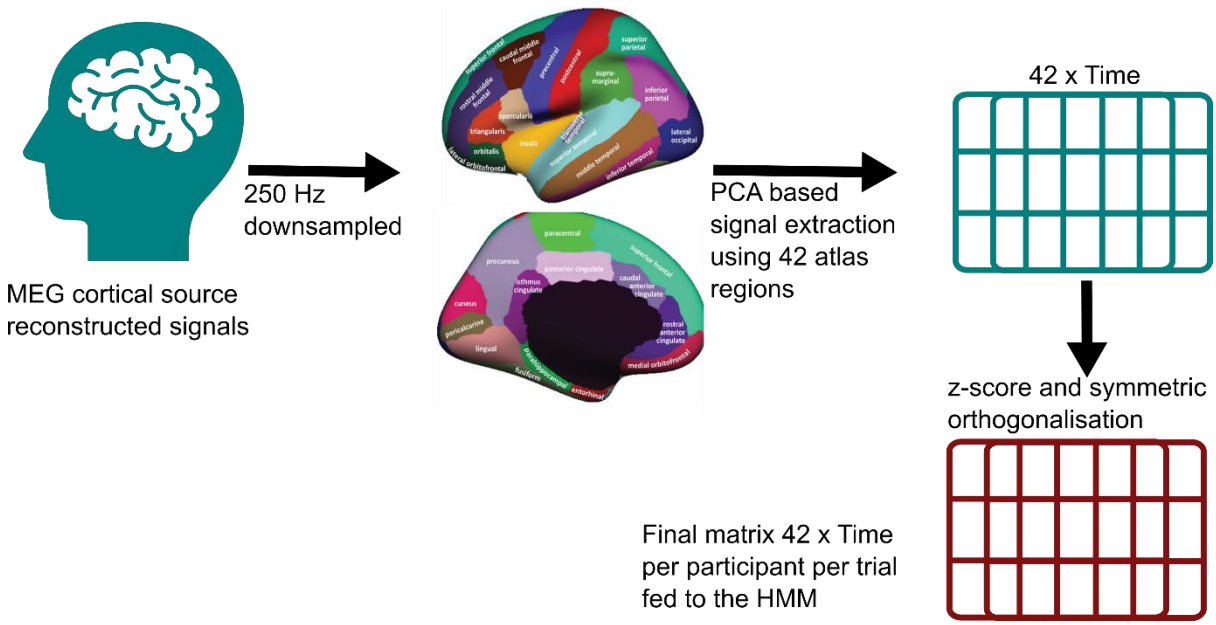


**Supplementary figure 8: A summary of the data processing pipeline for individual trials** (see Methods: Pre-processing).